Influences of Obstacle Factors on the Transmission Trends of Respiratory Infectious Diseases in Indoor Public Places

Ziwei Cui [1], Ming Cai [1], Yao Xiao [1*], Zheng Zhu [2], Gongbo Chen [3]

[1] School of Intelligent System Engineering, Sun Yat-Sen University, Shenzhen, Guangdong, China
[2] College of Civil Engineering and Architecture, Zhejiang University, Hangzhou, Zhejiang, China
[3] Guangdong Provincial Engineering Technology Research Center of Environmental and Health Risk Assessment; Department of Occupational and Environmental Health, School of Public Health, Sun Yat-sen University, Guangzhou, Guangdong, China

Abstract— Public facilities are important transmission places for respiratory infectious diseases (e.g., COVID-19), due to the frequent crowd interactions inside. Usually, changes of obstacle factors can affect the movements of human crowds and result in different epidemic transmission among individuals. Most related studies only focus on the specific scenarios, but the common rules are usually ignored for the impacts of obstacles' spatial elements on the epidemic transmission. To tackle these problems, this study aims to evaluate the impacts of three spatial factors of obstacles (i.e., size, quantity, and placement) on infection spreading trends in two-dimension, which can provide scientific and concise spatial design guidelines for indoor public places. Firstly, we used the obstacle area proportion as the indicator of the size factor, gave the mathematical expression of the quantity factor, and proposed the walkable-space distribution indicator to represent the placement factor. Secondly, two epidemic spreading indicators (i.e., daily new cases and people's average exposure risk) were estimated based on the fundamental model named exposure risk with the virion-laden droplets, which forecasted the disease spreading between individuals accurately. Thirdly, 120 indoor scenarios were built and simulated, based on which the value of independent and dependent variables can be measured. Besides, the Pearson correlation analysis and linear regression analysis were employed to examine the relations between obstacle factors and epidemic transmissions. Finally, several design guidelines were provided for policymakers to mitigate the disease spreading: minimizing the size of obstacles; increasing the obstacle quantity and adopting the uniform obstacle placement by lifting the smallest size of the walkable convex space.

Keywords: Obstacle Factors, Respiratory Infectious Diseases, Indoor Public Places, Spatial Design, Epidemic Spreading

1. Introduction

The unexpected Corona Virus Disease 2019 (COVID-19) epidemic has been a global concern in the past three years and has significantly impacted all aspects of the world [1,2]. The severe acute respiratory syndrome coronavirus 2 (SARS-CoV-2) causes this disease, and COVID-19 is a respiratory infectious disease (RID) with a high transmission rate [3]. RIDs including COVID-19, SARS and MERS [4] are harmful to public health, which always bring sequelae such as fatigue and dyspnea, and even cause the loss of life expectancy [5,6]. To reduce the potential risk of ongoing or re-emerging RIDs, the safety of individual staying spaces is of paramount concern [7,8]. Considering the fact that most individual contacts take place in indoor public places, recognizing the effective spatial setups in indoor public spaces with human crowds is essential for the prevention and control of RIDs [9-12].

There are some studies exploring the epidemic spreading in different scenarios with a moving crowd [2,13-20]. For example, Moritz et al. [13] conducted an experimental indoor mass gathering event under three different hygiene practices (i.e., no restrictions, moderate restrictions, and strong restrictions), and measured the contacts of each person

during the event with contact tracing devices. Then, based on the data, they simulated the exposure of individuals and evaluated the contributions of several preventive and control measures. The study by Ku et al. [14] focused on the resulting burden of COVID-19 in public transport. Specifically, they used the smart card data and real data on infected individuals to estimate the familiar stranger group, which was a specific public transportation user-frequently encounters. Furthermore, they simulated the spreading of the virus among public transportation users, and then predicted the transmission probability under the mandatory mask-wearing and social distancing. Mokhtari and Jahangir [2] used a university building as the case, and constructed a multi-objective optimization problem to find the optimum occupant distribution patterns. However, the spatial settings of obstacles are specified and fixed in these studies.

Recently, the influences of obstacles on the epidemic transmission have been explored from different perspectives. Under the constraints of non-pharmaceutical interventions such as maintaining safe social distance, the layout design of obstacles has been optimized to better prevent and control infection. Contardo and Costa [21] aimed to seek a layout that maximized the number of people that the restaurant can accommodate under satisfying social distancing constraints. Moreover, they analyzed whether adding space separators and considering the sitting sense of customers can increase the room capacity separately. Similarly, an equilateral triangle-based seat pattern was provided in symmetrical spaces to achieve maximum seating capacity under the physical distancing safety guidelines [22]. Mekawy and Gabr [23] presented a multi-objective optimization approach to mitigate the risks of infectious diseases' transmission in open-plan offices. In detail, they maximized the number of workers, window proximity score, "buzz score", and minimized "adjacency score" to respond to relative prevention and control measures. Differently, the impacts of the number of equal-size obstacles on disease spreading were studied by Azmi et al. [24]. To evaluate the best setup for the isolation room and the sanitizing machine for spreading disinfectant aerosol, they simulated the airflow in three rooms with different amounts of equal-size beds, respectively. Although these studies have provided useful findings for the spatial design in response to RIDs, they ignore details brought from the individual movements. Therefore, some researchers have coupled individual movement and spatial configuration management to study. Based on the space occupation and density of the moving crowd, Braidotti et al. [9] used pedestrian simulations to clarify the spatial problems for infection prevention in the ship environment. Then, an alternative layout was proposed to solve the above critical issues for the ship, but it did not apply to other scenarios. Xiao et al. [10] coupled the pedestrian dynamics and the modified susceptible–exposed–infectious model to decipher the spreading process of COVID-19, and they analyzed the resulting epidemic transmission in different scenarios (i.e., three closed rooms with different exits, three corridors with different settings of impassable railings, and three winding-queue configurations). However, their fundamental model was not tested with real-world data.

In sum, most previous studies focus on the placement of obstacles and the resulting epidemic transmission, but the physical mechanisms behind them are usually not clarified. Moreover, the impact of other obstacle factors, e.g., size and quantity, needs further evaluation. On the other hand, existing studies only pay attention to scenarios with the fixed function, e.g., office, hospital isolation room, and restaurant. However, exploring the obstacle factors' influences on a general indoor public place without considering its function are more useful. Based on this, scientific and concise obstacle adjustment advice can be concluded and further applied in different types of scenarios, which may contribute to the prevention and control of RIDs in the public health system.

This study aims to estimate the influences of the size, quantity, and placement of obstacles on the transmission trends in indoor public places, and clarify the mechanisms behind them. In reality, the spread of infection in indoor public places is rarely measured, and it is difficult to set obstacles flexibly in different scenarios to make them comparable. As a result, there is a lack of real-world data to achieve our goals. To tackle this issue, we attempt to obtain the basic data by simulating the epidemic transmission between individuals in indoor rooms with various obstacles. Therefore, we need a validated simulation fundamental model which can forecast the spreading trends of RIDs between moving individuals.

In addition, as the indicators of obstacle factors are the independent variables in the statistical analysis, it is necessary to find quantifiable indicators as dependent variables to represent the transmission trends.

The framework of our study is presented in Fig. 1, and it should be pointed that our study is conducted in two-dimension (2D). The rest of the paper is organized as follows. The methodology is presented in section 2. The simulation setups are illustrated in section 3, and the results are then reported in section 4. The in-depth discussions and future perspectives are reported in section 5. Finally, conclusions are provided in section 6.

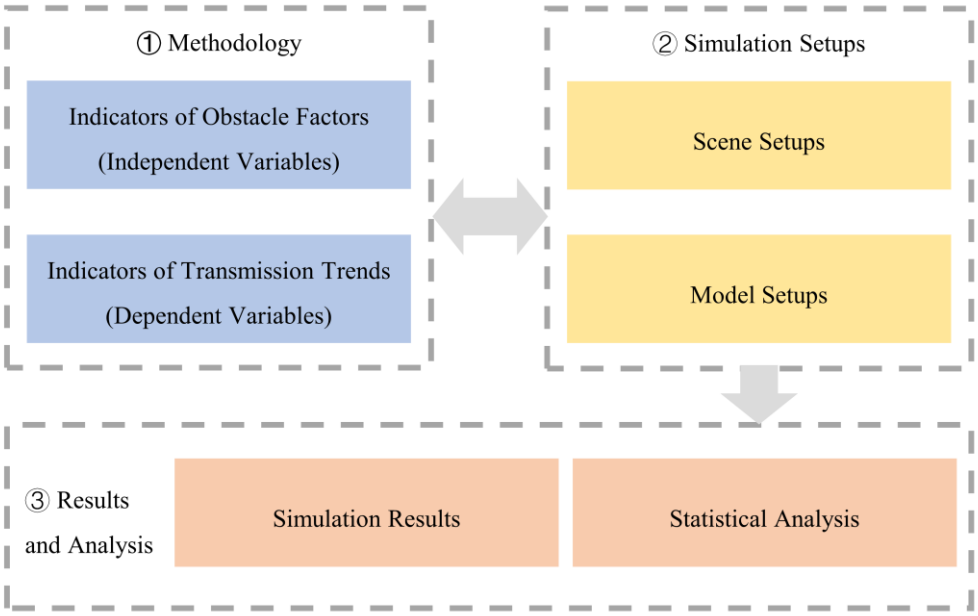

Fig. 1. There is the framework of our study.

2. Methodology

In this section, three indicators of obstacles factors are first defined, and then the adopted fundamental model is introduced, based on which two transmission trend indicators are determined.

2.1. Obstacle Factors

In a scenario, an obstacle is defined as a non-walkable object that does not intersect or tangent with others. The N^{Obs} refers to the quantity of obstacles in an indoor public place, and obstacles can be numbered as $\{1, \dots, n, \dots, N^{\mathrm{Obs}}\}$. The S_n^{Obs} is the size (2D area) of the n-th obstacle, and we have the total size of all obstacles as

$$S^{\mathrm{AllObs}} = \sum_{n=1}^{N^{\mathrm{Obs}}} S_n^{\mathrm{Obs}}. \tag{1}$$

Here, the dimensionless proportion R^{AllObs} is calculated as

$$R^{\mathrm{AllObs}} = \frac{S^{\mathrm{AllObs}}}{S^{\mathrm{Total}}} \times 100\%, \tag{2}$$

where S^{Total} is the size of the simulation room. Hence, the first and second obstacle indicators are determined mathematically, which are respectively the proportion of the obstacle size to the simulation space size R^{AllObs} and the quantity of obstacles N^{Obs}.

For the placement of obstacles, previous studies have explored based on the sizes and locations of obstacles [22-24]. In fact, individuals are moving in the walkable spaces, which vary with the layout of obstacles. It is more directly to analyze the variation of walkable spaces to find the effects and mechanism of the obstacle placement factor. To quantify the impact of obstacle placement and the resulting walkable area, we should describe the spaces quantitatively. Therefore, space Syntax,

which has successfully analyzed spatial relationships, is adopted here to express the space [25-28]. In Space Syntax, spaces can be defined in three ways: Convex Partitions, Axial Lines, and Isovists. As the indoor public place is focused in this study, the first way is used here as it is mainly used for small buildings and their interior space. Hence, continuous walkable space is divided into a series of convex spaces, and a convex space is defined as "one space where all points within this space are visible to one another" by Bill Hillier and his colleagues [27], see Fig. 2.

(a) (b)

Fig. 2. There are examples of the (a) convex and (b) non-convex spaces.

Moreover, Bill Hillier and his colleagues have suggested an algorithm for manually constructing a convex map: "Simply find the largest convex space and draw it in, then the next largest, and so on until all the space is accounted for.". However, there may be multiple convex spaces of the same size. Hence, for a given scenario, the algorithm cannot be used to represent a unique walkable convex map. For example, a scenario in Fig. 3(a) is a 22m×22m room with a 6m×6m obstacle at the geometric center. Each blue space in Fig. 3(b) can serve as the first walkable convex space, and their corresponding convex maps are different.

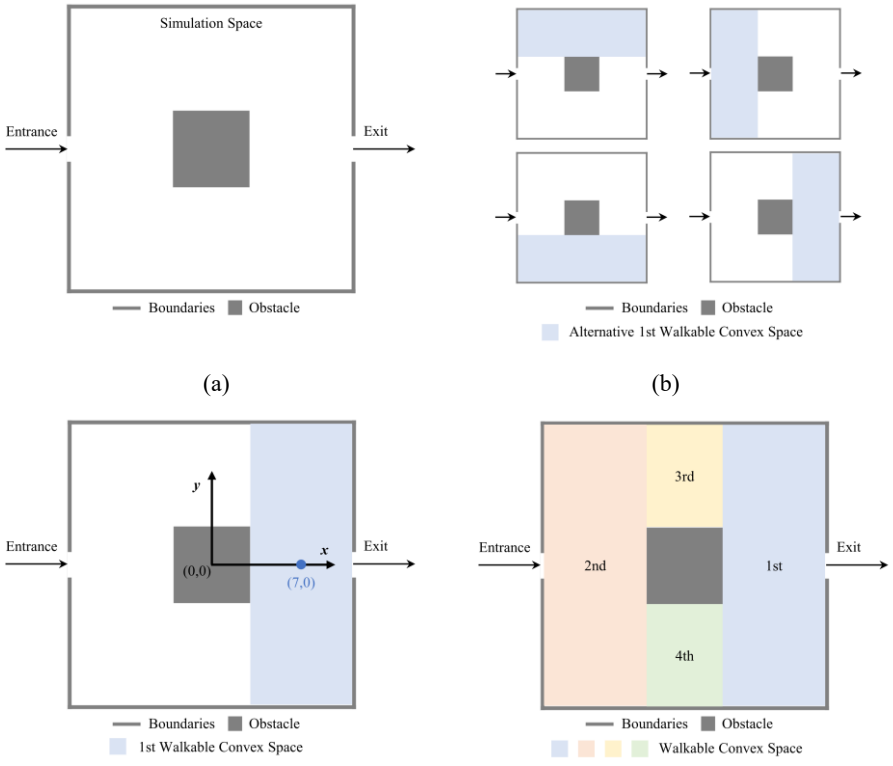

(a) (b)

(c) (d)

Fig. 3. In (a) a scenario, (b) there are four spaces that can be used as the first workable convex space in Hillier's method, and (c) a unique one can be determined as the first in our method. Then, a unique walkable convex map is obtained in (d) based on our method.

To tackle this issue, we first construct a rectangular coordinate system and then use greedy strategies to get the unique convex map for a scenario. The coordinate system has "x" and "y" axes, and its origin is the geometrical center of the simulation room. Moreover, the orientation of the "x" axis is the same as that of the pedestrian outflow. Then, the coordinate of the geometrical center in each convex walkable space is measured. Therefore, for a given scenario, we get started by finding the first convex space until all walkable areas have been added to the convex map. For each time, a unique convex space can be found and added to the map based on the following three steps.

- Step 1: Find the largest convex walkable space. If only one convex space with the largest size can be found, we draw it in the convex map; Otherwise, we transfer the spaces with the largest size to step 2.
- Step 2: Find the convex space with the maximum x-axis value among spaces from Step 1. If only one convex space with the largest size and the maximum x-axis value can be found, we draw it in the convex map; Otherwise, we transfer the spaces with the largest size and the maximum x-axis value to step 3.
- Step 3: Find the convex space with the maximum y-axis value among spaces from Step 2. As the geometric center coordinates of two convex spaces cannot be the same, the unique convex element can be identified and added to the convex map, as shown in Fig. 3(c).

Consequently, a unique convex map can be obtained for a constructed scenario (see Fig. 3(d)), and each component in the map is fixed. When there are M walkable convex spaces in a convex map, their determined sizes are respectively $\{S_1^{\mathrm{Con}}, \dots, S_m^{\mathrm{Con}}, \dots, S_M^{\mathrm{Con}}\}$.

Here, we propose the walkable-space distribution indicator D^{Con} to measure the variation of walkable spaces modified by the placement of obstacles. As the standard deviation is an index that represents the dispersion degree of the dataset, it can help measure the distribution of walkable space sizes in a convex map. Hence, the indicator D^{Con} is defined as the standard deviation of walkable convex spaces in a unique map and given as

$$D^{\mathrm{Con}} = \sqrt{\frac{\sum_{m=1}^{M}(S_m^{\mathrm{Con}} - \overline{S^{\mathrm{Con}}})^2}{M}}, \text{ where } \overline{S^{\mathrm{Con}}} = \frac{\sum_{m=1}^{M} S_m^{\mathrm{Con}}}{M}. \tag{3}$$

2.2. Fundamental Model and Transmission Trends Indicators

In forecasting the disease spreading between individuals, previous studies have integrated pedestrian dynamics into the epidemic spreading models [7,29-33]. These pedestrian-based epidemic models describe the disease transmission process with time-varying personal physical distances during individual movements. There are several alternative pedestrian-based epidemic models, such as the exposure risk with virion-laden droplets (ERD) model [7], the fixed exposure-risk unit (FERU) model [31], and the exposure risk with quality (ERQ) model [32]. As the ERD model has been verified with real-world data and exhibits superior prediction performance than FERU and ERQ models, it is adopted here as the fundamental model.

The ERD model [7] focuses on the typical symptom of most RIDs, i.e., coughing. The model has four components: individual movement, virion-laden droplet movement, individual exposure risk estimation, and prediction of transmission trends. Note that in the ERD model, the instantaneous exposure risk is defined as the possible maximal mass of droplets suffered when the individual and cough-generated droplets meet in the same place, and infectors' exposure risks are 0.

Firstly, based on the model inputs (i.e., number of individuals C^{total}, number of infectors among individuals C^{inf}, and mean dwell time of individuals T^{dwell}) and the pedestrian dynamic model (i.e., the social force model [34]), individuals' movements are reproduced in a general simulation place. Note that the social force model considers the realistic obstacle avoidance behaviors, and it can reasonably reproduce the people movements in the room with different obstacles. The velocity $\boldsymbol{v}_i$ of individual i (with a mass of m_i) at time t is estimated as

$$\frac{d\boldsymbol{v}_i}{dt} = \frac{\boldsymbol{F}_i^{\mathrm{drv}} + \sum_{i^{\mathrm{near}}} \boldsymbol{F}_{i,i^{\mathrm{near}}}^{\mathrm{ped}} + \sum_w \boldsymbol{F}_{i,w}^{\mathrm{obs}}}{m_i}, \tag{4}$$

where $\boldsymbol{F}_i^{\mathrm{drv}}$, $\sum_{i^{\mathrm{near}}} \boldsymbol{F}_{i,i^{\mathrm{near}}}^{\mathrm{ped}}$, $\sum_w \boldsymbol{F}_{i,w}^{\mathrm{obs}}$ are forces from goal, neighbors, and obstacles, respectively. Here, during the dwell time T^{dwell}, people would randomly adjust the goal, and the new goals are required to be away from obstacles. Once the staying time reaches the specified time T^{dwell}, the individual goal changes to the room exit. Therefore, the time series positions of each individual can be obtained.

Secondly, according to models and settings from literature [12,35], the transmission process of virion-laden droplets from a typical cough is simulated in a closed environment. The renormalization group (RNG) k-ε model is used as the turbulence model, and the discrete phase model is adopted for the droplet diffusion. Then, the velocity $\boldsymbol{u}_c$ of droplet c at time t is estimated as

$$\frac{d\boldsymbol{u}_c}{dt} = \boldsymbol{F}_D(\boldsymbol{u} - \boldsymbol{u}_c) + \boldsymbol{F}_g, \tag{5}$$

where $\boldsymbol{u}$ is the fluid phase velocity, $\boldsymbol{F}_D(\boldsymbol{u} - \boldsymbol{u}_c)$ is the Stokes drag force, and $\boldsymbol{F}_g$ is the gravitational force [36]. Thus, each cough droplet's time series positions and masses can be estimated.

Thirdly, outputs from the first two modules are coupled to estimate the $E_{i,j,g}$, i.e., the instantaneous exposure risk of individual i exposed to individual (infector) $j's$ g-th cough. Based on these, the exposure risk of individual i during the dwell time is measured as

$$E_i = \sum_{t=t_i^{\mathrm{enter}}}^{t_i^{\mathrm{enter}} + T_i^{\mathrm{dwell}}} \sum_{j=1}^{J(t)} \sum_{g=1}^{J_G(j,t)} E_{i,j,g}(t), \tag{6}$$

where t_i^{enter} is the place enter time, T_i^{dwell} is the dwell time of individual i, $J(t)$ denotes the number of infectors in the simulation scenario at time t, and $J_G(j,t)$ indicates the number of infectious coughs of the infector j at time t.

Finally, to predict the daily new cases C^{New}, the cut-line of high exposure risk α and the proportionality coefficient in the linear equation β should be estimated based on the real-world historical data. Besides, the number of susceptible individuals C^{sus} can be determined according to model inputs (=$C^{\mathrm{total}} - C^{\mathrm{inf}}$). Then, the number of high-risk exposed people C^{risk} during the simulation can be estimated as

$$C^{risk}(\alpha) = \sum_{i=1}^{C^{\mathrm{sus}}} \psi(E_i, \alpha), \ where \ \psi(E_i, \alpha) = \begin{cases} 1, \mathrm{if}\ E_i > \alpha \\ 0, \mathrm{otherwise} \end{cases}. \tag{7}$$

Therefore, the number of new cases C^{New} is represented by

$$C^{\mathrm{New}} = \beta * C^{\mathrm{risk}}(\alpha). \tag{8}$$

Based on the ERD model, for a scenario, we can predict the exposure risk of each individual E_i and the number of new cases C^{New}. As C^{New} is a direct and useful indicator to describe the disease spreading trends, it is adopted as a transmission indicator. Another indicator is people's average exposure risk E^{Ave}, which represents the general level of all visits' exposure risks in a scenario and is defined as

$$E^{\mathrm{Ave}} = \frac{\sum_i^{C^{\mathrm{sus}}} E_i}{C^{\mathrm{sus}}}, \tag{9}$$

where C^{sus} and E_i are the same as mentioned before.

3. Simulation Setups

3.1. Scenario Setups

A scenario consists of people and spaces. In this section, we first introduce the human simulation setups, and then determine the space simulation setups.

Both infectors and susceptible individuals are represented by a circle with a radius of 0.2 meters for simplification [34] (see Fig. 4). In the beginning, no individual is in the simulation space. Then, individuals enter the indoor room through the entrance in sequence with an average interval of 5 s, and leave through the room exit. In the dwell time, individuals follow the random walking pattern with the desired velocity of 1.34 m/s [31,34]. Besides, after entering the room, the infected individual averagely coughs every 15 s [31]. A cough's infectious distance is 1.70 m, and the infectious time follows a uniform distribution from 0 to 15 s [7].

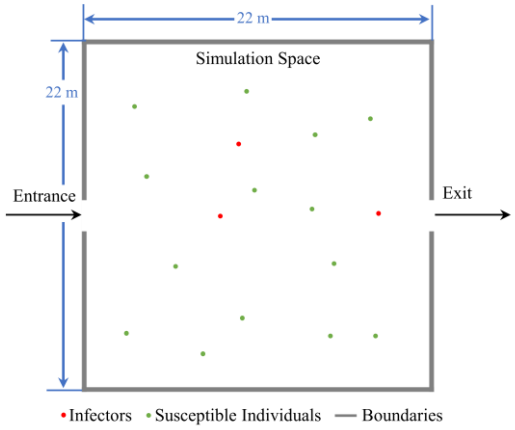

Fig. 4. There is the sketch map of the simulation people and room in the case.

We change the obstacles in the same simulation space to explore their factors influencing the transmission of RIDs. Herein, a fixed 22 m × 22 m indoor room is constructed as the simulation space, i.e., $S^{\mathrm{Total}} = 484\ \mathrm{m}^2$, and there is an entrance on one side of the room and an exit on the opposite side (see Fig. 4). There are two steps to determine the size, quantity, and placement of obstacles in each simulation scenario:

- Step 1: Determine the size and quantity of obstacles. The obstacle size indicator S^{AllObs} is formulated firstly. To clarify the impacts of the quantity of obstacles, an effective tool to separate the obstacle is needed. Here, a horizontal-vertical division rule is proposed for dividing square or rectangle obstacles, and it has four parameters: H^{cut}, V^{cut}, E^{cut}, and D^{cut}. Specifically, H^{cut} and V^{cut} are the number of divisions in the horizontal and vertical directions, respectively. E^{cut} is a binary variable, where $E^{\mathrm{cut}} = 1$ indicates the obstacle is divided equally and $E^{\mathrm{cut}} = 0$ represents unequal division. D^{cut} is the shortest distance between adjacent obstacles, whose value can be fixed or changeable in the division process.
- Step 2: Determine the placement of obstacles. After determining the size, quantity, and relative positions of obstacles, a minimum rectangle that can cover all obstacles can be found. Then, the geometrical center G^{AllObs} of the rectangle is uniquely determined when the placement of obstacles in the room is fixed. Thus, when we build a coordinate system with "x" and "y" axes, whose origin is the geometrical center of the simulation space G^{Room}, the obstacle positions can be confirmed based on the accurate coordinate of G^{AllObs}.

According to the above steps, we set 5 groups with different total obstacle sizes (i.e., $S^{\mathrm{AllObs}} = 36\ \mathrm{m}^2$, $64\ \mathrm{m}^2$, $100\ \mathrm{m}^2$, $144\ \mathrm{m}^2$, $196\ \mathrm{m}^2$, respectively), and obstacles are all square before segmentation. Besides, we set $H^{\mathrm{cut}} \in [0,1,2,3]$ and $V^{\mathrm{cut}} \in [0,1,2]$ in each group with the same S^{AllObs}, and explore the simple situation when $E^{\mathrm{cut}} = 1$ and $D^{\mathrm{cut}} = 2.0$ m. For example, there are 12 patterns in the group with $S^{\mathrm{AllObs}} = 36\ \mathrm{m}^2$ (see Fig. 5), and six same obstacles are obtained in the pattern with $H^{\mathrm{cut}} = 3$ and $V^{\mathrm{cut}} = 2$. Hence, independent variables of N^{Obs} and R^{AllObs} in each scenario can be measured. Moreover, we set two coordinates of G^{AllObs} for each pattern to explore the influence of obstacle placement, and the first coordinate is $(0,0)$. To ensure that all obstacles are in the simulation room, for each group with $S^{\mathrm{AllObs}} = 36\ \mathrm{m}^2$, $64\ \mathrm{m}^2$, $100\ \mathrm{m}^2$, $144\ \mathrm{m}^2$, $196\ \mathrm{m}^2$, the second coordinate is set as $(0,-5)$, $(0,-4)$, $(0,-3)$, $(0,-2)$, and $(0,-1)$, respectively. For example, for the pattern $H^{\mathrm{cut}} = 3$ and $V^{\mathrm{cut}} = 2$ when $S^{\mathrm{AllObs}} = 36$

m^2, two obstacle placements in the simulation space are shown in Fig. 6. Based on these, the independent variable D^{Con} in each scenario can be estimated.

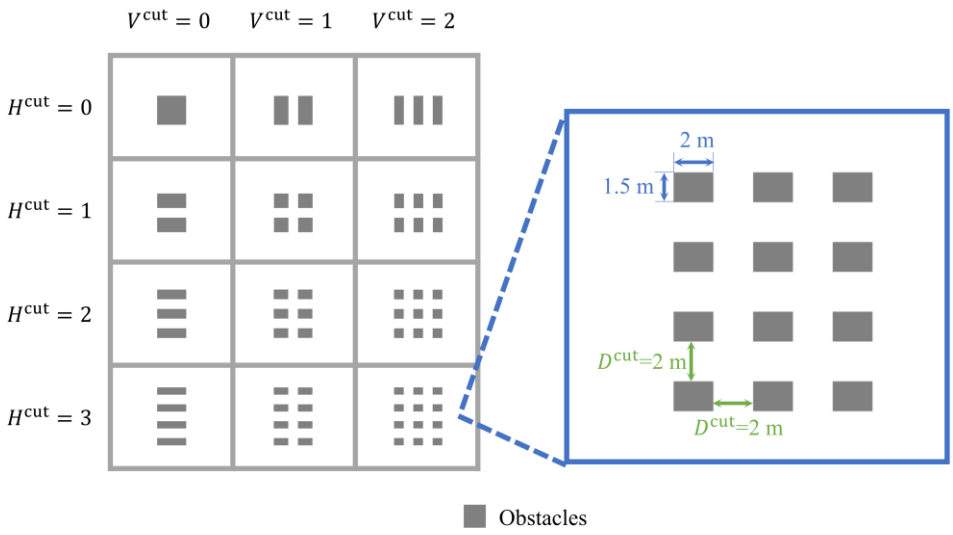

Fig. 5. The division results based on the horizontal-vertical division rule when $S^{\mathrm{non}} = 36\ \mathrm{m}^2$.

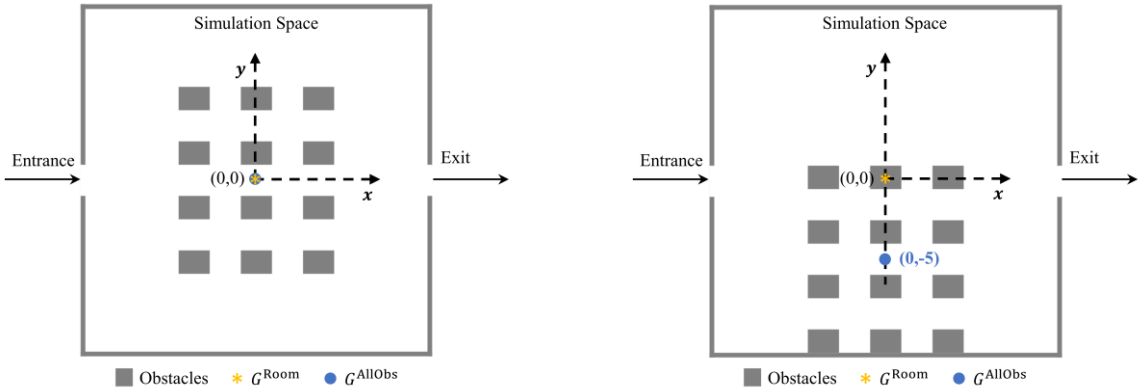

Fig. 6. When $S^{\mathrm{non}} = 36\ \mathrm{m}^2$, $H^{\mathrm{cut}} = 3$, and $V^{\mathrm{cut}} = 2$, there are two layouts with different positions of obstacle.

In sum, there are 5 groups with different obstacle sizes, 12 patterns in each group, and 2 coordinates in each pattern to estimate the placement. Thus, there are $5{\times}12{\times}2 = 120$ samples collected in this case. Each scenario is simulated at least three times to ensure that the standard deviation of their resulting new cases is smaller than C^{NewStd}, and the average experimental results are taken as the final values. In this case, C^{NewStd} is set as 600 through numerous tests. Each scenario is denoted by a sequence of intervention codes in the "S^{AllObs}-[H^{cut}, V^{cut}]-G^{AllObs}" format. For instance, Scenario #36-[3,2]-(0,-5) represents the scenario when the size of obstacle S^{AllObs} is 36 m^2, the position of obstacle geometrical center G^{AllObs} is $(0,-5)$, and the pattern in the horizontal-vertical division rule is $H^{\mathrm{cut}} = 3$ and $V^{\mathrm{cut}} = 2$. Fig. 7 shows the configuration of all 24 scenarios when S^{AllObs} is 36 m^2.

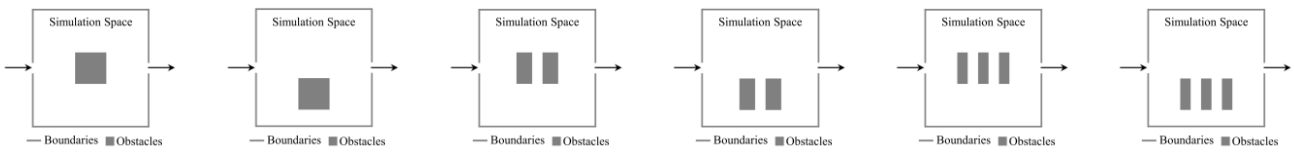

#36-[0,0]-(0,0) #36-[0,0]-(0,-5) #36-[0,1]-(0,0) #36-[0,1]-(0,-5) #36-[0,2]-(0,0) #36-[0,2]-(0,-5)

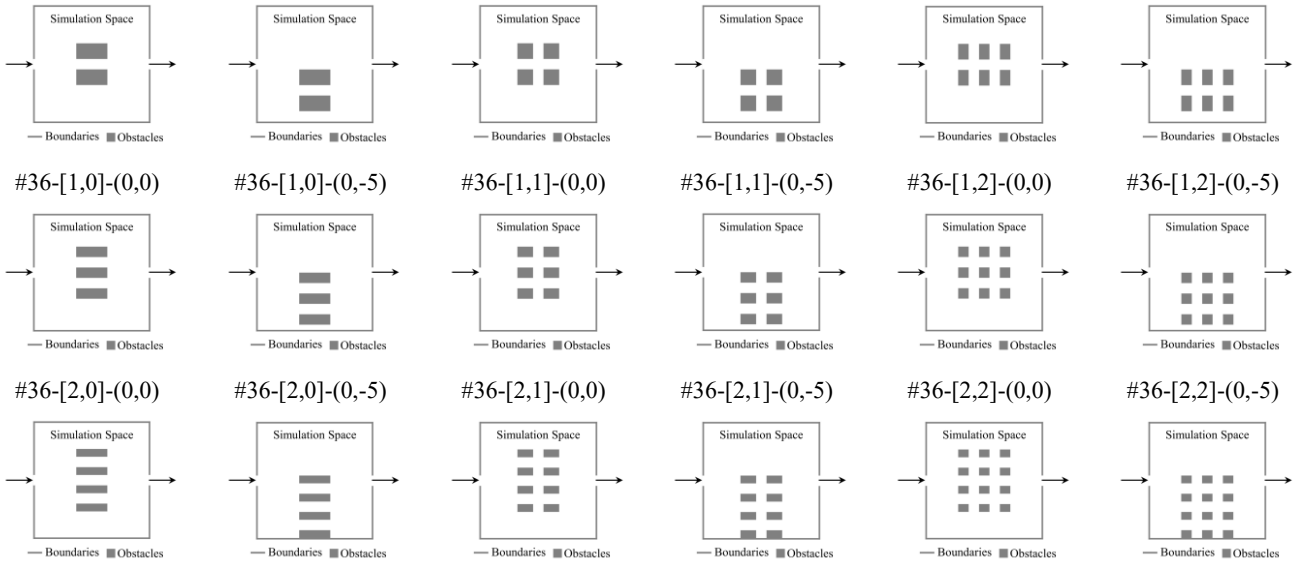

Fig. 7. There are 24 scenarios when S^{AllObs} is 36 m^2.

3.2. Model Setups

As introduced in section 2.2, there are three main individual inputs in the ERD model: number of individuals C^{total}, number of infectors among individuals C^{inf}, and mean dwell time T^{dwell}. Since the impacts of obstacle factors are explored in this study, the fixed values of model inputs are enough. Thus, we use data from the United States (U.S.) during the spreading of COVID-19 on June 5th, 2020, and there are C^{total} =257,177,921 [37,38], C^{inf}=1,759,672 [39], and T^{dwell} =25 minutes [31,38]. Meanwhile, according to the research of [7], to reduce the computational cost, C^{total} and C^{inf} are scaled down with a proportion $\rho = 4.07 \times 10^{-5}$ for simulation, and the model results C^{New} are expanded with the same proportion after the simulation; the appropriate value of parameters α and β are set as 7.00 μg and 6.20×10^{-4}, respectively.

4. Results and Analysis

4.1. Simulation Results

Obstacle factors are calculated based on the simulation setups, and transmission trend indicators are collected from the simulation outputs. Based on the simulation results, the descriptive statistics of the independent and dependent variables are reported in Table 1.

Table 1

Descriptive statistics of independent and dependent variables.

Variables	Number of samples	Min. Values	Max. Values	Mean	Standard Deviation
Independent variables					
R^{AllObs}	120	7.40%	40.50%	22.30%	11.80%
N^{Obs}	120	1.00	12.00	5.00	3.18
D^{Con}	120	15.01	102.85	46.37	20.04
Dependent variables					
C^{New}	120	22,560	42,781	30,238	4,697
E^{Ave} (μg)	120	3.00	4.78	3.64	0.42

4.2. Statistical Analysis

4.2.1 Influences of the Size of Obstacles

According to the simulation results of 120 scenarios, the number of new cases C^{New} and the average individual exposure risk E^{Ave} vary with the proportion of the obstacle size to the simulation space size R^{AllObs} in Fig. 8, respectively.

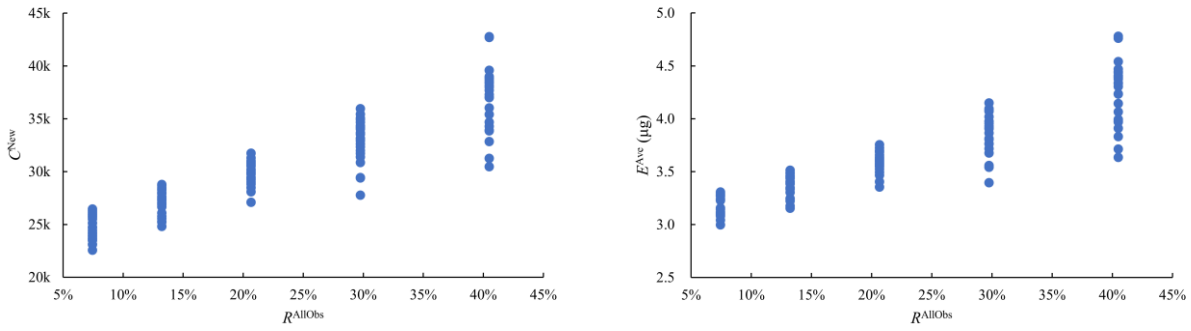

(a) (b)

Fig. 8. (a) C^{New} and (b) E^{Ave} vary with R^{AllObs}.

After using standardized data with the min-max scaler method, correlation analysis is adopted to explore the relationships between the size attribute and the epidemic transmission. Firstly, we test the distributions of variables with the Shapiro-Wilk test, and all variables obey normal distribution characteristics. Secondly, the Pearson coefficient is applied for correlation analysis, and the results are reported in Table 2.

Table 2

Correlation between R^{AllObs} and dependent variables.

Variables	C^{New}	E^{Ave}
R^{AllObs}	**0.917****	**0.906****

Note: * p<0.05, ** p<0.01.

Based on Table 2, there is a linear interrelationship between R^{AllObs} and C^{New}, and the same in R^{AllObs} and E^{Ave}. Hence, the disease spreading indicators (C^{New} and E^{Ave}) can be modelled as the linear function of the obstacle attributes R^{AllObs}. The mathematical functions are given as

$$C^{\mathrm{New}} = a_1 R^{\mathrm{AllObs}} + b_1 \tag{10}$$

and

$$E^{\mathrm{Ave}} = a_2 R^{\mathrm{AllObs}} + b_2, \tag{11}$$

where R^{AllObs}, C^{New}, and E^{Ave} are constructed variables in section 3; a_1 and a_2 are the coefficients of each independent variable; b_1 and b_2 are the intercepts in each function. We employ the ordinary least square method to estimate coefficients, and the results are demonstrated in Table 3.

We test the heteroscedasticity for the model constructed in Table 3 to incorporate potential estimation problems. Based on the White test, the χ^2 of regression models with dependent variable C^{New} and E^{Ave} are 23.878 (p-value = 0.000**) and 29.616 (p-value = 0.000**), respectively. Thus, there is heteroscedasticity in models built. To track this issue, we add the robust standard error (see Table 4).

Table 3

Summary of linear regression results.

Variables	Dependent Variable C^{New}				Dependent Variable E^{Ave} (μg)			
	Coefficient	St. Err.	t-stat	p-value	Coefficient	St. Err.	t-stat	p-value
R^{AllObs}	0.596	0.024	24.939	0.000**	0.591	0.025	23.273	0.000**
Constant	0.112	0.014	8.149	0.000**	0.096	0.015	6.627	0.000**
R-Squared	0.841		——		0.821		——	
Adjusted R-Squared	0.839		——		0.820		——	
F-statistic	621.960		——		541.624		——	
Prob(F-statistic)	0.000		——		0.000		——	
Durbin-Watson stat	1.630		——		1.658		——	

Note: * p<0.05, ** p<0.01.

Table 4

Summary of linear regression results with the robust standard error.

Variables	Dependent Variable C^{New}				Dependent Variable E^{Ave} (μg)			
	Coefficient	Robust St. Err.	t-stat	p-value	Coefficient	Robust St. Err.	t-stat	p-value
R^{AllObs}	**0.596**	0.030	20.159	**0.000****	**0.591**	0.032	18.570	**0.000****
Constant	0.112	0.010	11.183	0.000**	0.096	0.010	9.739	0.000**
R-Squared	**0.841**		——		**0.821**		——	
Adjusted R-Squared	0.839		——		0.820		——	
F-statistic	406.394		——		344.848		——	
Prob(F-statistic)	0.000		——		0.000		——	
Durbin-Watson stat	1.630		——		1.658		——	

Note: * p<0.05, ** p<0.01.

According to Table 4, the R-squared value of 0.841 and 0.821 indicated that the transmission variables C^{New} and E^{Ave} can be explained by variables of R^{AllObs} (84.1% and 82.1%), respectively, while other variables explain the rest. Besides, there is a significant and positive influence of the R^{AllObs} on epidemic transmission variables (C^{New} and E^{Ave}), and we have

$$C^{\mathrm{New}} = 0.596R^{\mathrm{AllObs}} + 0.112 \tag{12}$$

and

$$E^{\mathrm{Ave}} = 0.591R^{\mathrm{AllObs}} + 0.096. \tag{13}$$

Hence, with the growth of the obstacle size, more and more individuals will be infected, and the average exposure risk of the global will increase. Therefore, decreasing the size of obstacles is beneficial for reducing epidemic transmission.

4.2.2 Influences of the Quantity of Obstacles

To control the influence of the size factor, we analyze the quantity attribute in each size group. Here, the number of new cases C^{New} and the average individual exposure risk E^{Ave} change with the quantity of obstacles N^{Obs} in each group with the same R^{AllObs}, respectively (see Fig. 9).

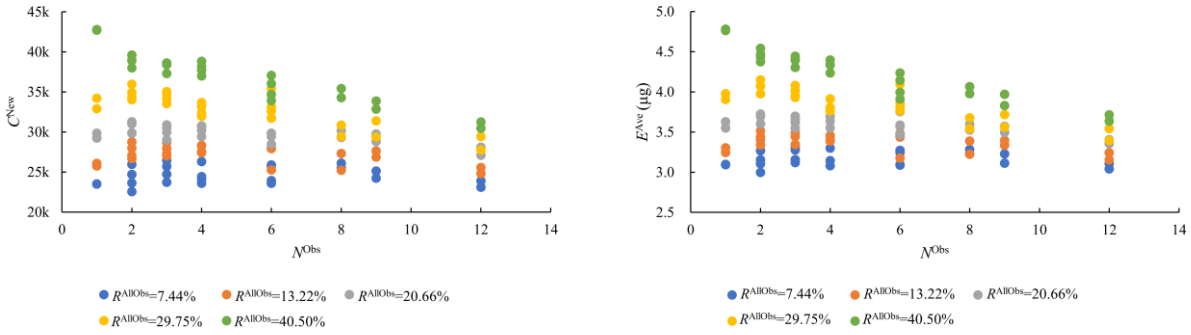

(a) (b)

Fig. 9. (a) C^{New} and (b) E^{Ave} change with N^{Obs} in each group with the same R^{AllObs}.

We use the min-max scaler method to standardize data, based on which the correlation analysis is performed. The distribution of N^{Obs} in each size group is tested to obey the normal distribution according to the Shapiro-Wilk test. Then, we adopt the Pearson coefficient for analysis, and the results are introduced in Table 5.

Table 5

Correlation between N^{Obs} and dependent variables.

Group	Correlation Between N^{Obs} and C^{New}	Correlation Between N^{Obs} and E^{Ave}
R^{AllObs}=7.44%	0.024	-0.015
R^{AllObs}=13.22%	-0.398	-0.418*
R^{AllObs}=20.66%	**-0.582****	**-0.670****
R^{AllObs}=29.75%	**-0.844****	**-0.856****
R^{AllObs}=40.50%	**-0.937****	**-0.942****

Note: * p<0.05, ** p<0.01.

As introduced in Table 5, when R^{AllObs} is large enough (i.e., $R^{AllObs} = 20.66\%, 29.75\%, 40.50\%$), the linear relationships between N^{Obs} and transmission indicators (C^{New} and E^{Ave}) are respectively observed in each size group. Therefore, in a size group with $R^{AllObs} \in \{20.66\%, 29.75\%, 40.50\%\}$, the linear mathematical functions are given as

$$C^{New} = a_3 N^{Obs} + b_3 \quad (14)$$

and

$$E^{Ave} = a_4 N^{Obs} + b_4, \quad (15)$$

where N^{Obs}, C^{New}, and E^{Ave} are constructed variables in section 3; a_3 and a_4 are the coefficients of each independent variable; b_3 and b_4 are the intercepts in each function. Then, based on the ordinary least square method, regression results are reported in Table 6.

Table 6

Summary of linear regression results when $R^{AllObs} = 20.66\%, 29.75\%, 40.50\%$.

Group	Variables	Dependent Variable C^{New}			Dependent Variable E^{Ave}		
		Coefficient	t-stat (p-value)	R-Squared	Coefficient	t-stat (p-value)	R-Squared
R^{AllObs}=20.66%	N^{Obs}	**-0.448**	**-3.361 (0.003**)**	**0.339**	**-0.559**	**-4.231 (0.000**)**	**0.449**
	Constant	0.745	12.067 (0.000**)		0.798	13.018 (0.000**)	
R^{AllObs}=29.75%	N^{Obs}	**-0.756**	**-7.386 (0.000**)**	**0.713**	**-0.781**	**-7.766 (0.000**)**	**0.733**
	Constant	0.884	18.644 (0.000**)		0.893	19.141 (0.000**)	
R^{AllObs}=40.50%	N^{Obs}	**-0.804**	**-12.572(0.000**)**	**0.878**	**-0.839**	**-13.199(0.000**)**	**0.888**
	Constant	0.813	27.442 (0.000**)		0.831	28.175 (0.000**)	

Note: * p<0.05, ** p<0.01.

In addition, the results of the White test show that there is no heteroscedasticity in the constructed regression models in Table 6. Results of Table 6 indicate that the R-squared of the linear regression increases with the growth of R^{AllObs}. The R-squared is respectively as high as 0.878 and 0.888 with dependent variables C^{New} and E^{Ave} in the size group $R^{\mathrm{AllObs}} = 40.50\%$, which implies that N^{Obs} can explain 87.8% of the changes in C^{New} and 88.8% of the variations in E^{Ave}. Moreover, there are significant and negative effects of the N^{Obs} on the epidemic transmission variables when $R^{\mathrm{AllObs}} = 20.66\%,\ 29.75\%$, and 40.50%. Therefore, once the obstacle size is large enough, increasing the obstacle quantity can decrease the disease infections.

4.2.3 Influences of the Placement of Obstacles

Similarly, we introduce the transmission indicators C^{New} and E^{Ave} vary with the standard deviation of walkable convex spaces D^{Con} in each size group to remove the effects of the size factor, as shown in Fig. 10.

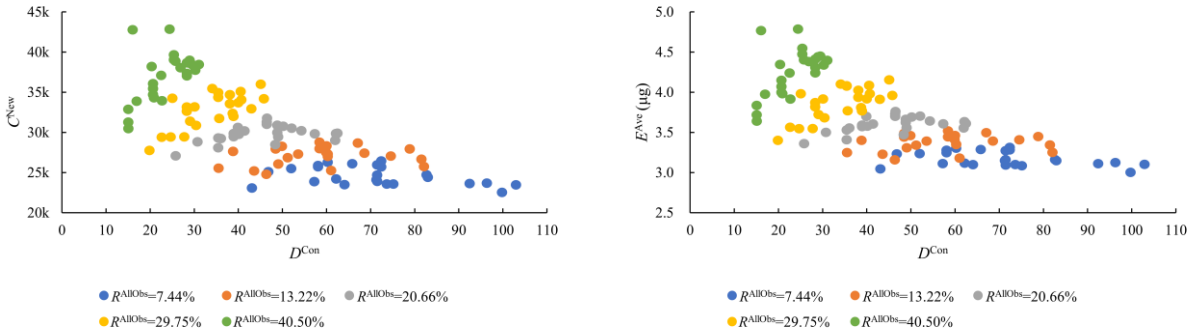

(a) (b)

Fig. 10. (a) C^{New} and (b) E^{Ave} vary with D^{Con} in each group with the same R^{AllObs}.

After using the min-max scaler method to standardize data, the correlation analysis is carried out. In each size group, D^{Con} is tested to obey normal distribution in each size group with the Shapiro-Wilk test. Hence, the Pearson coefficient is used, and the results are introduced in Table 7.

Table 7

Correlation between D^{Con} and dependent variables.

Group	Correlation Between D^{Con} and C^{New}	Correlation Between D^{Con} and E^{Ave}
R^{AllObs}=7.44%	-0.398	-0.365
R^{AllObs}=13.22%	0.146	0.158
R^{AllObs}=20.66%	**0.408***	**0.485***
R^{AllObs}=29.75%	**0.697****	**0.692****
R^{AllObs}=40.50%	**0.544****	**0.573****

Note: * p<0.05, ** p<0.01.

According to Table 7, the significant and positive linear relations between D^{Con} and infection spreading variables are obtained when R^{AllObs} is larger enough (i.e., $R^{\mathrm{AllObs}} = 20.66\%, 29.75\%, 40.50\%$). Thus, in the size group with $R^{\mathrm{AllObs}} \in \{20.66\%, 29.75\%, 40.50\%\}$, the linear mathematical functions are defined as

$$C^{\mathrm{New}} = a_5 D^{\mathrm{Con}} + b_5 \tag{16}$$

and

$$E^{\mathrm{Ave}} = a_6 D^{\mathrm{Con}} + b_6, \tag{17}$$

where D^{Con}, C^{New}, and E^{Ave} are constructed variables in section 3; a_5 and a_6 are the coefficients of each independent variable; b_5 and b_6 are the intercepts in each function. Consequently, regression results combining the ordinary least square method are demonstrated in Table 8.

Table 8

Summary of linear regression results when $R^{\mathrm{AllObs}} = 20.66\%, 29.75\%, 40.50\%$.

Group	Variables	Dependent Variable C^{New}			Dependent Variable E^{Ave}		
		Coefficient	t-stat (p-value)	R-Squared	Coefficient	t-stat (p-value)	R-Squared
R^{AllObs}=20.66%	D^{Con}	**0.344**	**2.099 (0.048*)**	**0.167**	**0.444**	**2.603 (0.016*)**	**0.236**
	Constant	0.395	3.996 (0.001**)		0.353	3.428 (0.002**)	
R^{AllObs}=29.75%	D^{Con}	**0.656**	**4.560 (0.000**)**	**0.486**	**0.664**	**4.490 (0.000**)**	**0.478**
	Constant	0.252	2.869 (0.009**)		0.247	2.738 (0.012*)	
R^{AllObs}=40.50%	D^{Con}	**0.423**	**3.038 (0.006**)**	**0.296**	**0.463**	**3.280 (0.003**)**	**0.328**
	Constant	0.303	3.594 (0.002**)		0.287	3.354 (0.003**)	

Note: * p<0.05, ** p<0.01.

Moreover, results of the White test imply that there is no heteroscedasticity in the constructed models in Table 8. As shown in Table 8, with the increase of R^{AllObs}, the R-squared value increased firstly and then decreased in models with the same dependent variable. The maximum R-squared value appears in the group with R^{AllObs}=29.75%, which is respectively 0.486 for the dependent variable C^{New} and 0.478 for the dependent indicator E^{Ave}. Thus, changes of C^{New} and E^{Ave} can be explained by variable D^{Con} up to 48.6% and 47.8%, respectively. Furthermore, the significant and positive relations between D^{Con} and infection spreading variables are found in Table 8. Hence, if the obstacle size is large enough, decreasing the standard deviation of walkable convex spaces resulting from the obstacle placement can reduce the epidemic infections.

5. Discussions and Future Perspectives

Building upon the importance of space design in COVID-19 transmission, the impacts of obstacle factors are evaluated using statistical analysis, from which we draw three conclusions if other factors remain constant: 1) the large obstacle area proportion facilitates epidemic transmission; when the size of obstacles is fixed and large enough, 2) the growing quantity of obstacles and 3) the lower value of walkable-space distribution indicator reduce epidemic spreading. In this section, we further discuss the reasons and the scope of applications of these findings.

In a scenario, with the growth of the obstacle size, the walkable space reduces, and the people density (= the size of walkable space/number of individuals in the simulation room) increases accordingly, as shown in Fig. 11. Hence, infectious spaces constructed by infectors are denser, and there is a higher possibility that susceptible individuals arrive at the infectious areas and facilitates epidemic spreading. In addition, the higher density brings a lower velocity[40,41], which results in a longer time to pass through the infectious space and then increases the transmission. As the desired velocity is a fixed setup in our cases, we can further explore the impacts of the various crowd walking speeds on the infection spread as in previous studies [10,15].

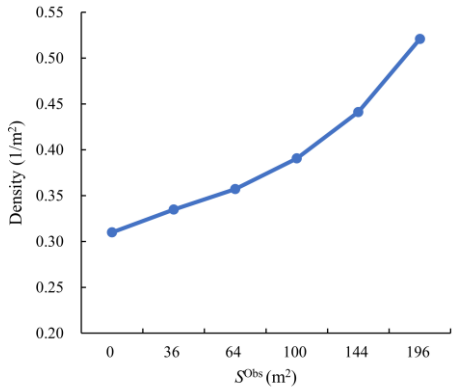

Fig. 11. Density varies with the total size of obstacles.

For the second and third findings, once the obstacle size is large enough, increasing the obstacle quantity N^{Obs} or decreasing the value of the walkable-space distribution indicator D^{Con} brings a reduction in epidemic infections. In addition, as reported in Table 9, there is a significant and negative relation between N^{Obs} and D^{Con} in each size group. Hence, there is a possible reason for the second finding: the growing quantity of obstacles decreases the transmission with the reduction of walkable-space distribution indicator D^{Con}. Besides, the walkable-space distribution indicator D^{Con} represents the obstacle placement. Thus, we will explain why the indicator D^{Con} affects the epidemic spreading trends as follows. According to the definition of the indicator D^{Con} in equation (3), a larger value of D^{Con} brings a lower bound of the walkable convex space size, which results in more gathering and congestion as they always happen in small walkable spaces. The gathering and congestion in the crowd lead to a longer time of accompanying motion between susceptible individuals and infectors, which increases the transmission. Therefore, if the obstacle is large enough, the more uniform distribution of walkable convex space lowers the epidemic spreading. It should be noted that when the total obstacle size is too small, the transmission trends affected by the quantity or placement factors are minor, which is unlike to cause significant variations.

Table 9

Correlation between variables N^{Obs} and D^{Con} in each group with the same R^{AllObs}.

Group	Correlation Between N^{Obs} and D^{Con}
R^{AllObs}=7.44%	-0.729**
R^{AllObs}=13.22%	-0.717**
R^{AllObs}=20.66%	-0.729**
R^{AllObs}=29.75%	-0.735**
R^{AllObs}=40.50%	-0.704**

Note: * p<0.05, ** p<0.01.

In the simulation setups, the shortest distance between adjacent obstacles D^{cut} is fixed as 2m. Here, we use scenario #100-[1,2]-(0,0) as the base and explore different layouts with D^{cut} is 1m, 3m, and 4m. These layouts are shown in Fig. 12(a), and corresponding simulation results indicate that the diverse values of D^{cut} bring various D^{Con} and further reflect the transmission.

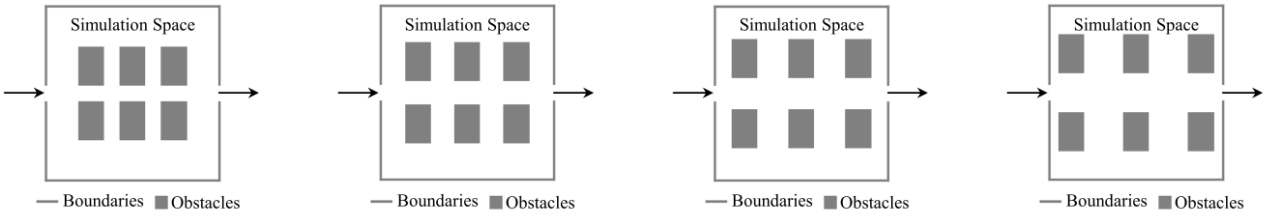

(a)

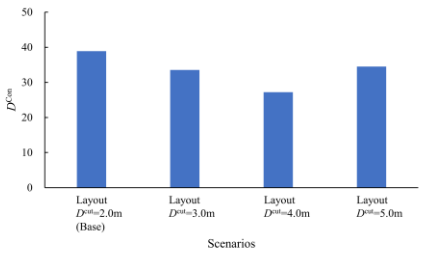

(b)

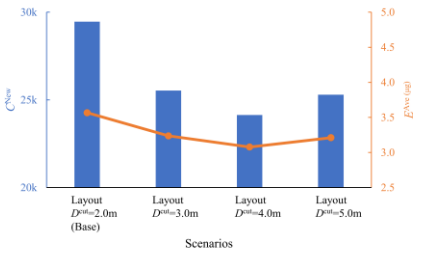

(c)

Fig. 12. Using the scenario #100-[1,2]-(0,0) as the base, there are (a) different layouts with D^{cut} is 1m, 3m, and 4m, and their corresponding (b) D^{Con} and (c) transmission indicators are reported.

Meanwhile, several limitations need to be further studied. Firstly, due to a lack of real-world data to achieve the research goal, we use the simulated data based on the ERD fundamental model. As the ERD model has been quantitatively calibrated and validated through the macroscopic real-life data, the prediction transmission trends are reliable to some extent, and the results can be applied for scenario investigation and comparison. Once we get the real-world data in the future, the findings in this paper can be further validated. Secondly, in our cases, individuals walk freely inside the simulated space, but people's diverse behavior and the points of interest in the scenario are ignored. For example, in a cinema, visitors stay in a fixed seat for a long time instead of walking randomly. Thus, individuals moving patterns in various scenarios should be considered in the future, which helps determine the customized prevention and control measures for a scenario. Thirdly, the shape of the pedestrian and the obstacle are respectively fixed as the circle and the rectangular for simplicity. However, both the pedestrian and the obstacle in real scenarios have various shapes and thus bring more dynamic properties. Therefore, further studies can be carried out in applying the realistic object features.

6. Conclusions

In this paper, the association between obstacle factors (i.e., size, quantity, and placement) and RIDs transmission trends were examined. Firstly, we constructed three spatial indicators of obstacle factors in 2D: the obstacle area proportion, the quantity of obstacles, and the walkable-space distribution indicator. Note that the last factor was built based on the walkable space, which represented the influence of obstacle placement instead of using the obstacle locations in previous studies, and helped explore the mechanism behind the impacts because individuals were moving in the walkable space. Then, we used the ERD model as the foundation, and selected daily new cases and people's average exposure risk as infection indicators. Finally, we built 120 scenarios with different sizes, quantities, and placements for simulation, and corresponding results were fed to the statistical analysis, including correlation analysis and linear regression.

There are three main findings in our study. 1) Increasing the obstacle size enhances the epidemic spreading by lifting the probability of susceptible individuals reaching the infectious walkable spaces and the time of passing through the space. Once the obstacle size is large enough, 2) increasing the obstacle quantity and 3) optimizing the obstacle placement can decrease the infections by reducing the walkable convex space with a small size where gathering and congestion always happen.

Therefore, in daily presentation and control of RIDs, we should minimize obstacles in the room. However, if the obstacles are indispensable and large, dividing obstacles into more sub-blocks and putting them uniformly can help decrease the epidemic transmission.

Appendix A

There are five different sizes of obstacles in our study, i.e. 36 m^2, 64 m^2, 100 m^2, 144 m^2, 196 m^2. As the scenarios with the size of 36 m^2 have been shown in Fig. 7, the rest scenarios are illustrated in Fig. A1.

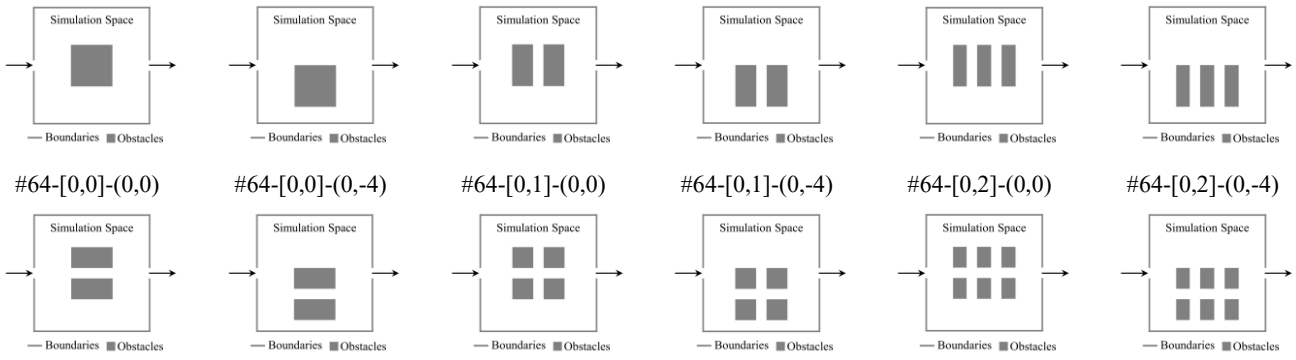

#64-[1,0]-(0,0)

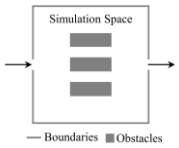

#64-[1,0]-(0,-4)

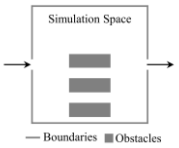

#64-[1,1]-(0,0)

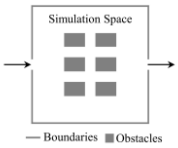

#64-[1,1]-(0,-4)

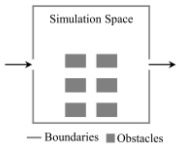

#64-[1,2]-(0,0)

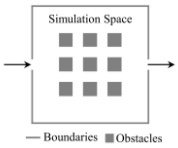

#64-[1,2]-(0,-4)

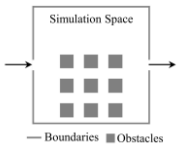

#64-[2,0]-(0,0)

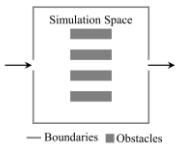

#64-[2,0]-(0,-4)

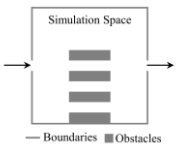

#64-[2,1]-(0,0)

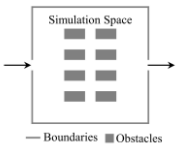

#64-[2,1]-(0,-4)

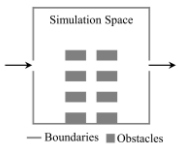

#64-[2,2]-(0,0)

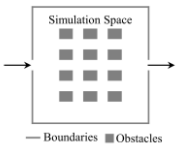

#64-[2,2]-(0,-4)

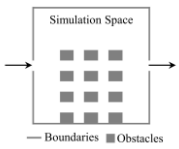

#64-[3,0]-(0,0)

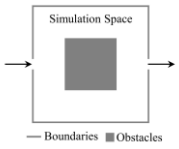

#64-[3,0]-(0,-4)

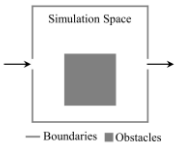

#64-[3,1]-(0,0)

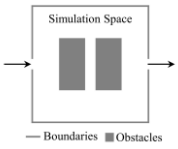

#64-[3,1]-(0,-4)

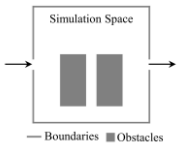

#64-[3,2]-(0,0)

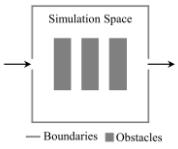

#64-[3,2]-(0,-4)

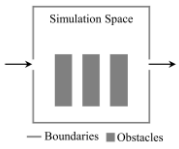

#100-[0,0]-(0,0)

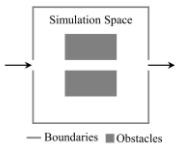

#100-[0,0]-(0,-3)

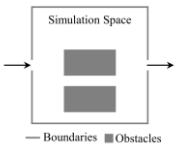

#100-[0,1]-(0,0)

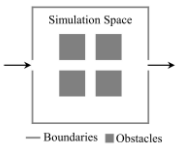

#100-[0,1]-(0,-3)

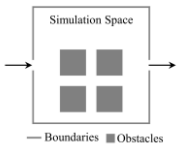

#100-[0,2]-(0,0)

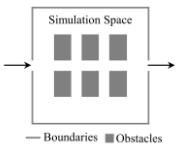

#100-[0,2]-(0,-3)

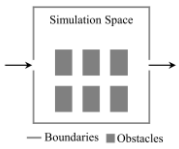

#100-[1,0]-(0,0)

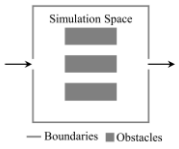

#100-[1,0]-(0,-3)

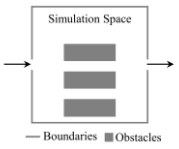

#100-[1,1]-(0,0)

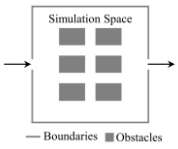

#100-[1,1]-(0,-3)

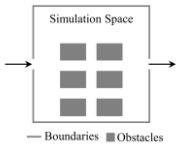

#100-[1,2]-(0,0)

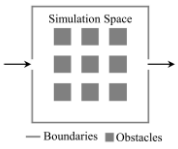

#100-[1,2]-(0,-3)

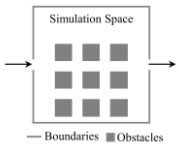

#100-[2,0]-(0,0)

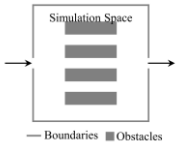

#100-[2,0]-(0,-3)

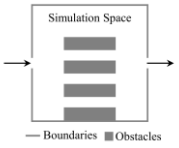

#100-[2,1]-(0,0)

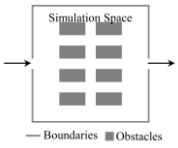

#100-[2,1]-(0,-3)

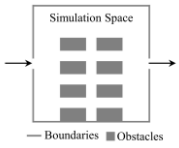

#100-[2,2]-(0,0)

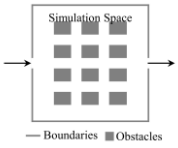

#100-[2,2]-(0,-3)

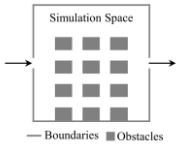

#100-[3,0]-(0,0)

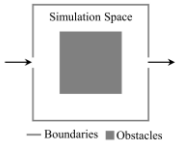

#100-[3,0]-(0,-3)

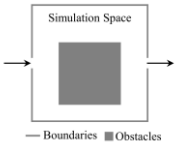

#100-[3,1]-(0,0)

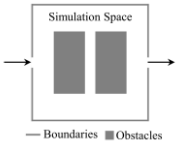

#100-[3,1]-(0,-3)

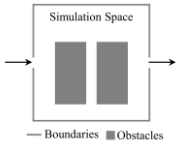

#100-[3,2]-(0,0)

#100-[3,2]-(0,-3)

#144-[0,0]-(0,0)

#144-[0,0]-(0,-2)

#144-[0,1]-(0,0)

#144-[0,1]-(0,-2)

#144-[0,2]-(0,0)

#144-[0,2]-(0,-2)

#144-[1,0]-(0,0)

#144-[1,0]-(0,-2)

#144-[1,1]-(0,0)

#144-[1,1]-(0,-2)

#144-[1,2]-(0,0)

#144-[1,2]-(0,-2)

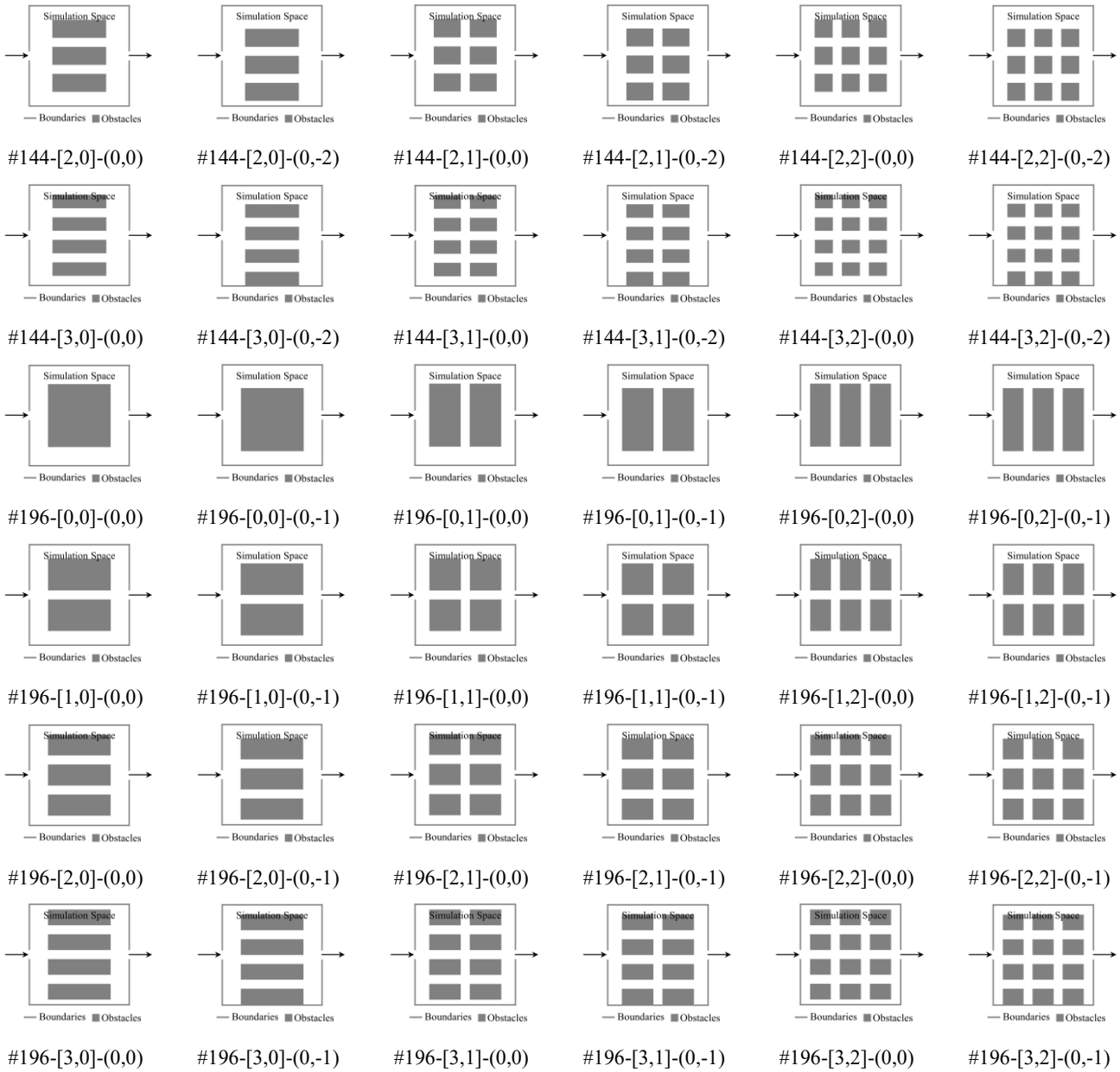

Fig. A1. There are scenarios with the obstacle size of 64 m^2, 100 m^2, 144 m^2, 196 m^2.

Conflict of Interest Statement

None declared.

Funding Sources

This work was supported by the National Natural Science Foundation of China (Grant No. 72101276), Shenzhen Science and Technology Innovation Committee (Grant No. GXWD 20200830165201001), and the Fundamental Research Funds for the Central Universities (Grant No. 22qntd1710).

References

[1] A.M. Hassan, N.A. Megahed, COVID-19 and urban spaces: A new integrated CFD approach for public health opportunities, Build. Environ. 204 (2021) 108131.

[2] R. Mokhtari, M.H. Jahangir, The effect of occupant distribution on energy consumption and COVID-19 infection in buildings: A case study of university building, Build. Environ. 190 (2021) 107561.

[3] S. Flaxman, S. Mishra, A. Gandy, H.J.T. Unwin, T.A. Mellan, H. Coupland, C. Whittaker, H. Zhu, T. Berah, J.W. Eaton, Estimating the effects of non-pharmaceutical interventions on COVID-19 in Europe, Nature. 584 (7820) (2020) 257-261.

[4] A.K. Melikov, COVID-19: Reduction of airborne transmission needs paradigm shift in ventilation, Build. Environ. 186 (2020) 107336.

[5] G. Huang, F. Guo, Loss of life expectancy due to respiratory infectious diseases: Findings from the global burden of disease study in 195 countries and territories 1990–2017, Journal of Population Research (2022) 1-43.

[6] Y. Xie, B. Bowe, Z. Al-Aly, Burdens of post-acute sequelae of COVID-19 by severity of acute infection, demographics and health status, Nat. Commun. 12 (1) (2021) 1-12.

[7] Z. Cui, M. Cai, Y. Xiao, Z. Zhu, M. Yang, G. Chen, Forecasting the transmission trends of respiratory infectious diseases with an exposure-risk-based model at the microscopic level, Environ. Res. (2022) 113428.

[8] P. Chen, D. Zhang, J. Liu, I.Y. Jian, Assessing personal exposure to COVID-19 transmission in public indoor spaces based on fine-grained trajectory data: A simulation study, Build. Environ. (2022) 109153.

[9] L. Braidotti, S. Bertagna, M. Dodero, M. Piu, A. Marinò, V. Bucci, Identification of measures to contain the outbreaks on passenger ships using pedestrian simulations, Procedia Computer Science. 200 (2022) 1565-1574.

[10] T. Xiao, T. Mu, S. Shen, Y. Song, S. Yang, J. He, A dynamic physical-distancing model to evaluate spatial measures for prevention of Covid-19 spread, Physica a. 592 (2022) 126734.

[11] H. Qian, T. Miao, L. Liu, X. Zheng, D. Luo, Y. Li, Indoor transmission of SARS‐CoV‐2, Indoor Air. 31 (3) (2021) 639-645.

[12] Z.T. Ai, A.K. Melikov, Airborne spread of expiratory droplet nuclei between the occupants of indoor environments: A review, Indoor Air. 28 (4) (2018) 500-524.

[13] S. Moritz, C. Gottschick, J. Horn, M. Popp, S. Langer, B. Klee, O. Purschke, M. Gekle, A. Ihling, F.D.L. Zimmermann, R. Mikolajczyk, The risk of indoor sports and culture events for the transmission of COVID-19, Nat. Commun. 12 (1) (2021).

[14] D. Ku, C. Yeon, S. Lee, K. Lee, K. Hwang, Y.C. Li, S.C. Wong, Safe traveling in public transport amid COVID-19, Science advances. 7 (43) (2021) g3691.

[15] W. Garcia, S. Mendez, B. Fray, A. Nicolas, Model-based assessment of the risks of viral transmission in non-confined crowds, Safety Sci. 144 (2021) 105453.

[16] B. Qi, J. Tan, Q. Zhang, M. Cao, X. Wang, Y. Zou, Unfixed movement route model, non-overcrowding and social distancing reduce the spread of COVID-19 in sporting facilities, Int. J. Env. Res. Pub. He. 18 (15) (2021) 8212.

[17] R. Löhner, H. Antil, High fidelity modeling of aerosol pathogen propagation in built environments with moving pedestrians, Int. J. Numer. Meth. Bio. 37 (3) (2021).

[18] Q. Xu, M. Chraibi, On the effectiveness of the measures in supermarkets for reducing contact among customers during COVID-19 period, Sustainability-Basel. 12 (22) (2020) 9385.

[19] H. Salmenjoki, M. Korhonen, A. Puisto, V. Vuorinen, M.J. Alava, Modelling aerosol-based exposure to SARS-CoV-2 by an agent based Monte Carlo method: Risk estimates in a shop and bar, Plos One. 16 (11) (2021) e260237.

[20] T. Lu, Y. Zhao, P. Wu, P. Zhu, Dynamic analysis of single-file pedestrian movement with maintaining social distancing in times of pandemic, Journal of Statistical Mechanics. 2021 (9) (2021) 93402.

[21] C. Contardo, L. Costa, On the optimal layout of a dining room in the era of COVID-19 using mathematical optimization, arXiv (2021).

[22] L. Bañón, C. Bañón, Improving room carrying capacity within built environments in the context of COVID-19, Symmetry. 12 (10) (2020) 1683.

[23] M. Mekawy, M.A. Gabr, Against a workplace contagion: a digital approach to support hygiene-conscious office space planning, Open House International. 46 (3) (2021) 391-400.

[24] N.Z.E. Azmi, M.I.P. Hidayat, A.D. Pramata, Numerical simulation of effects of number of beds and presence of aerosol

flow from sanitation machine to air circulation in hospital isolation room of COVID-19 patients, Materials Research Communications. 2 (1) (2021).

[25] S.Y. Bapir, S.M. Kareem, Covid-19 and functionality: By providing social distancing of indoor common spaces in residential building, Journal of Studies in Science and Engineering. 1 (1) (2021) 36-45.

[26] S.Y. Bapir, S.M. Kareem, How to limit the spread of covid-19 in residential buildings: Erbil city as a case study, Design Engineering (2021) 2635-2647.

[27] B. Hillier, J. Hanson, The social logic of space, Cambridge university press, Cambridge, UK, 1984.

[28] N. Abdul Nasir, A. Hassan, F. Khozaei, M. Abdul Nasir, Investigation of spatial configuration management on social distancing of recreational clubhouse for COVID-19 in Penang, Malaysia, International Journal of Building Pathology and Adaptation (2020).

[29] D. Kim, A. Quaini, Coupling kinetic theory approaches for pedestrian dynamics and disease contagion in a confined environment, Mathematical Models and Methods in Applied Sciences. 30 (10) (2020) 1893-1915.

[30] E. Ronchi, R. Lovreglio, EXPOSED: An occupant exposure model for confined spaces to retrofit crowd models during a pandemic, Safety Sci. 130 (2020) 104834.

[31] Y. Xiao, M. Yang, Z. Zhu, H. Yang, L. Zhang, S. Ghader, Modeling indoor-level non-pharmaceutical interventions during the COVID-19 pandemic: a pedestrian dynamics-based microscopic simulation approach, Transport Policy. 109 (2021) 12-23.

[32] E. Hernández-Orallo, A. Armero-Martínez, How human mobility models can help to deal with covid-19, Electronics. 10 (1) (2020) 33.

[33] P.S. Abdul Salam, W. Bock, A. Klar, S. Tiwari, Disease contagion models coupled to crowd motion and mesh-free simulation, Mathematical Models and Methods in Applied Sciences. 31 (06) (2021) 1277-1295.

[34] D. Helbing, P. Molnar, Social force model for pedestrian dynamics, Physical review E. 51 (5) (1995) 4282.

[35] L. Borro, L. Mazzei, M. Raponi, P. Piscitelli, A. Miani, A. Secinaro, The role of air conditioning in the diffusion of Sars-CoV-2 in indoor environments: A first computational fluid dynamic model, based on investigations performed at the Vatican State Children's hospital, Environ. Res. 193 (2021) 110343.

[36] L. Zhang, Y. Li, Dispersion of coughed droplets in a fully-occupied high-speed rail cabin, Build. Environ. 47 (2012) 58-66.

[37] Maryland Transportation Institute and Center for Advanced Transportation Technology Laboratory at the University of Maryland, Trips by distance – national. 2021. https://data.bts.gov/Research-and-Statistics/Trips-by-Distance-National/6ced-86in (accessed June 27th, 2021).

[38] L. Zhang, A. Darzi, S. Ghader, M.L. Pack, C. Xiong, M. Yang, Q. Sun, A. Kabiri, S. Hu, Interactive COVID-19 Mobility Impact and Social Distancing Analysis Platform, Transport. Res. Rec. (2021) 862848922, 10.1177/03611981211043813.

[39] Centers for Disease Control and Preventions, Covid-19 case surveillance public data access, summary, and limitations. 2021. https://data.cdc.gov/Case-Surveillance/United-States-COVID-19-Cases-and-Deaths-by-State-o/9mfq-cb36 (accessed June 22nd, 2021).

[40] L.D. Vanumu, K. Ramachandra Rao, G. Tiwari, Fundamental diagrams of pedestrian flow characteristics: A review, European transport research review. 9 (4) (2017) 1-13.

[41] S. Cao, A. Seyfried, J. Zhang, S. Holl, W. Song, Fundamental diagrams for multidirectional pedestrian flows, Journal of Statistical Mechanics: Theory and Experiment. 2017 (3) (2017) 33404.